inorganics

MDPI

Article

Positive Influence of Oxalate and Cyanate on the Supercapacitance Performance of V/Co 2D-Nanolayered Structures

Osama Saber [1,2,*], Sajid Ali Ansari [1,*], Nazish Parveen [3], Nagih M. Shaalan [1,4], Aya Osama [1] and Mostafa Osama [1]

[1] Department of Physics, College of Science, King Faisal University, P.O. Box 380, Al-Ahsa 31982, Saudi Arabia; nmohammed@kfu.edu.sa (N.M.S.); ayamohamed19984@yahoo.com (A.O.); mostafa.osama8664@gmail.com (M.O.)
[2] Egyptian Petroleum Research Institute, Nasr City, P.O. Box 11727, Cairo 11765, Egypt
[3] Department of Chemistry, College of Science, King Faisal University, P.O. Box 380, Al-Ahsa 31982, Saudi Arabia; nislam@kfu.edu.sa
[4] Physics Department, Faculty of Science, Assiut University, Assiut 71516, Egypt
* Correspondence: osmohamed@kfu.edu.sa (O.S.); sansari@kfu.edu.sa (S.A.A.); Tel.: +966-13-589-9440 (O.S.)

Abstract: Two-dimensional (2D) nanolayered and nanohybrid structures, which are composed of different species of organic anions and multi-valence inorganic cations, are considered favorable in the field of energy storage for use as supercapacitors. In this study, host–guest interactions were used to build a series of these nanohybrids. The host was the layered double hydroxides of vanadium–cobalt (V/Co) nanolayers with different molar ratios. Cyanate was used as a guest to design a V/Co supercapacitor with a 2D-nanolayered structure. In addition, oxalate was used as a new additive to improve the performance of the V/Co supercapacitor. X-ray diffraction, infrared spectroscopy, thermal analyses, and scanning electron microscopy confirmed the formation of the nanolayered structures of cyanate-V/Co. In the case of the oxalate-V/Co nanostructures, a new phase of cobalt oxalate was produced and combined with the nanolayered structure to build a 3D porous structure. A three-assembly electrode system was used to study the electrochemical supercapacitive behavior of the cyanate-V/Co and oxalate-V/Co nanolayered structures. The results indicated that the OXVC-20 electrode possessed the highest specific capacitance as compared to that of the OXVC-16 and CNOVC electrodes. An excellent stability performance of up to 91% after various charge–discharge cycles was detected for the optimum case. Because of the positive effect of oxalate on the supercapacitance performance of the V/Co supercapacitor, it is suggested as a new track for building active electrodes for high-performance supercapacitor applications.

Keywords: V/Co nanolayers; 2D organic–inorganic electrodes; oxalate-V/Co nanohybrids; charge–discharge method; cyclic voltammetry

Citation: Saber, O.; Ansari, S.A.; Parveen, N.; Shaalan, N.M.; Osama, A.; Osama, M. Positive Influence of Oxalate and Cyanate on the Supercapacitance Performance of V/Co 2D-Nanolayered Structures. *Inorganics* **2023**, *11*, 458. https://doi.org/10.3390/inorganics11120458

Academic Editor: Chek Hai Lim

Received: 20 October 2023
Revised: 13 November 2023
Accepted: 20 November 2023
Published: 26 November 2023

1. Introduction

Layered double hydroxides (LDHs) have an inorganic structure and comprise a group of nanolayered materials. They have attracted growing interest due to their potential applications in catalysis [1], separation [2], drug delivery [3], and energy storage [4]. Among them, the use of LDHs as supercapacitor materials in the field of energy storage has been a hotspot of research [5]. LDH materials consist of di- and trivalent metals combined in hydroxide nanolayers, which are cationic in nature and thus capable of intercalation anions [6]. It is well established that the properties of materials are strongly connected to their shape, size, and elemental composition. Many researchers have reported that the synthesis of LDHs with a large specific surface area, such as a three-dimensional (3-D) layered structure, can be used to significantly improve the performance of materials [7,8]. Therefore, it has become the pursuit of materials scientists. Depending on the structure

of the LDH, supercapacitor materials with high performance, obtained through the building of 3D-nanolayered structures, have been increasingly reported in the literature. The hydrothermal and co-precipitation methods [9,10], in addition to template and microwave-assisted techniques [11,12], have used a metal ion solution and an alkaline precipitant as raw materials for the design of high-performance supercapacitor materials. Among the different transition metals, nickel and cobalt have attracted attention for the design of 3D-nanolayered materials for supercapacitor applications because of their high stability, elevated specific capacitance, and high electrical conductivity. For instance, 3D flower-like nanostructured NiCo LDHs with a supercapacitance performance of 1187 F g^{-1} at 1 A g^{-1} were prepared by Zhou et al. [13]. Jing and coworkers described the synthesis of a Ni-Co LDH by using a one-step alternative voltage electrochemical technique for the supercapacitor electrode material. These Ni-Co LDH nanoflakes had an interlayer spacing of 0.767 nm and attained a maximum specific capacitance of 1372 F g^{-1} at 1 A g^{-1} [14]. Hou et al. fabricated a self-assembled urchin-like Ni-Co LDH structure for producing supercapacitor electrode materials with a specific capacitance of 808.4 C g^{-1} at 1 A g^{-1} [15]. Similarly, Jiang et al. used ZIF-67 as a sacrificial template for synthesizing Ni-Co LDH nano-cages to produce a supercapacitor with the electrochemical performance of 1203 F g^{-1} at 1 A g^{-1} [16]. Although the produced supercapacitors achieved high performance, their preparation methods are still complex and need to be improved. This means that the preparation techniques of 3D NiCo-LDH supercapacitor materials need to be developed to become simpler and produce superior properties.

Supercapacitor electrodes based on LDH materials have been studied in detail. However, studies on vanadium-based LDH electrodes are scarce. Tyagi et al. used carbon cloth as a support for the prepared NiV-LDHs to produce a high-performance supercapacitor with a specific capacity of 1226 C g^{-1} [17]. Therefore, vanadium plays an important role in improving the performance of supercapacitors because of its unique properties, such as multiple oxidation states and high energy density [18]. In this way, lithium/sodium ion and zinc ion batteries were developed using vanadium-based electrodes [19–22]. The energy density of supercapacitors was improved, and the conductivity of the electrodes was increased by introducing vanadium to the active materials of the supercapacitor electrodes [23].

By preparing novel ultrathin NiV-LDHs, Zhou and his colleagues [24] produced electrodes with high specific capacitance. However, these electrodes showed poor stability. The researchers improved cycling stability by converting NiV-LDHs to NiV-S LDHs through an ion exchange reaction (OH replaced by S). Gonçalves et al. [25] studied NiV-LDHs using hybrid supercapacitors.

Recently, many researchers [26,27] have focused on V-LDHs that contain more than two metals for producing high-supercapacitor electrode materials. Wu et al. [27] prepared nanosheet arrays of the V-doped NiCo-LDH displaying the highest performance with a specific capacitance of 2960 F g^{-1} at a current density of 1 A g^{-1}. In 2021, Lee et al. attempted to prepare a cobalt–vanadium LDH for a high-energy-density hybrid supercapacitor. However, their XRD results showed different phases of cobalt hydroxides failing in the preparation of a cobalt–vanadium LDH [28]. In addition to dual transition metal cations, the incorporation of anions and other useful additives to transition metal hydroxides can also enhance the efficiency of the supercapacitors [29–37].

In this study, we synthesized the 2D-nanolayered structure of cyanate-V/Co LDH through the thermal decomposition of urea. Cyanate anions were used as pillars among the nanolayers. Then, a 2D-nanolayer-structure V/Co was developed through the growth of a new phase of cobalt oxalate to produce a 3D nanostructure using oxalate anions instead of cyanate anions. By studying the electrochemical supercapacitive behaviors of the different nanostructures of cyanate-V/Co and oxalate-V/Co, this work provides a new method for synthesizing 3D-structured LDH materials with high supercapacitor performance and excellent stability and further indicates that the growth of the oxalate

phase on 2D nanostructures to synthesize 3D porous structures based on LDHs is feasible and promising.

2. Results and Discussion

2.1. Chemical and Elemental Analysis

The chemical analysis of CNOVC LDH indicated that the percentages of carbon, hydrogen, and nitrogen were 2.4, 2, and 1.5, respectively. These results suggest that CNOVC LDH contains cyanate in addition to traces of carbonate anions as guests. Elemental chemical analysis results (as determined by Inductively Coupled Plasma (ICP)) for CNOVC LDH showed that the V/Co mole ratio was 1/4, agreeing with the mole ratio existing in the starting solution.

2.2. X-ray Diffraction

Figure 1a indicates the X-ray diffraction pattern of the product CNOVC after a reaction time of 6 h. It reveals only two clear peaks at 2θ = 11.28° and 23.18°, agreeing with the interlayered spacing (d_{003} and d_{006}) of 0.788 nm and 389 nm, respectively. By comparing these peaks with the structure of natural hydrotalcite and the main peaks of the conventional layered double hydroxides, it can be seen that these peaks indicate the growth of the nanolayered structure of CNOVC [38,39].

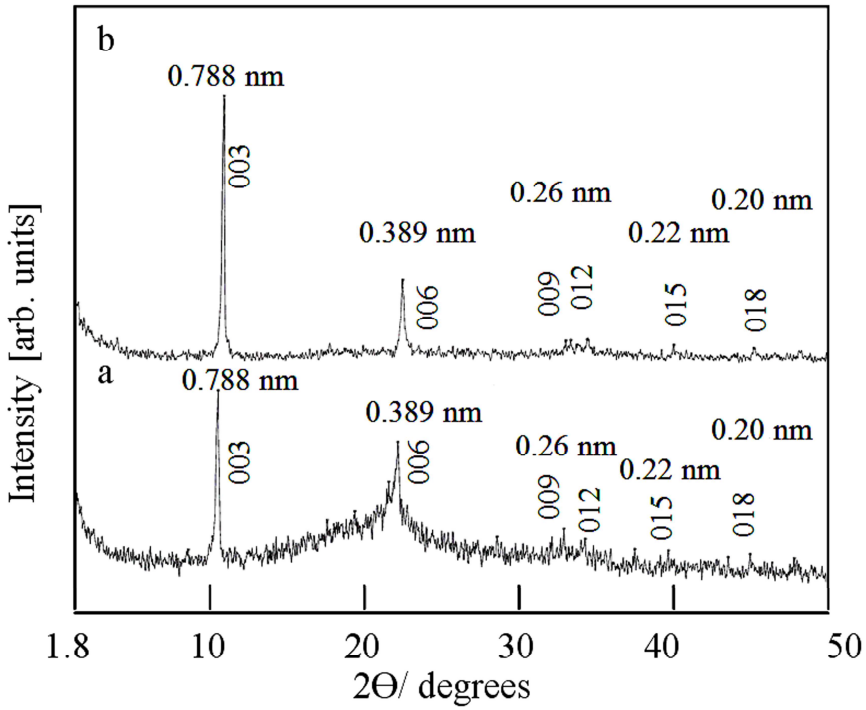

Figure 1. X-ray diffraction of CNOVC after different reaction times: (**a**) 6 h and (**b**) 15 h.

This indication was confirmed by increasing the reaction time to 15 h because Figure 1b shows clear reflections of hkl planes (003), (006), and (009). X-ray diffraction of CNOVC showed a strong and sharp peak at 0.788 nm. The comparison between the reflections of the main planes (003), (006), and (009) showed that d_{003} (0.788 nm) ≈ 2 × d_{006} (0.389 nm) ≈ 3 × d_{009} (0.26 nm). This means that the CNOVC layers were highly packed in an ordered form along axis c. The lattice parameter "c" was estimated as 3 × d_{003} = 2.364 nm. Compared with the lattice parameters that were published for synthetic and natural hydrotalcites and the well-known LDH materials in the carbonate form (JCPDS file No. 37-629) and (JCPDS file No. 48-1022), this value shifted from c = 2.2575 nm to 2.364 nm [40]. This shift may be caused by the inclusion of cyanate anions between the CNOVC layers. Also, Figure 1b shows the reflections of the non-base planes (012), (015), and (018) at 0.25 nm, 0.22 nm,

and 0.20 nm, respectively. The growth of the non-base and the base planes of CNOVC indicate the positive effect of raising the reaction time to produce the V/Co LDH crystals and confirm a complete formation of the layered structure of V/Co LDH.

In order to study the effect of intercalation of oxalate anions on the LDH structure, the vanadium precursor was changed from vanadyl dichloride to vanadyl oxalate. Figure 2a shows the X-ray diffraction pattern of the product OXVC-20 after a reaction time of 6 h. The characteristic peaks of a layered structure disappeared, and weak peaks were observed at 2θ = 18.58°, 22.56°, 24.41°, and 29.81°. This means that the nanolayered structure became disordered and a new phase started to grow. After increasing the reaction time to 15 h, a series of weak peaks started to grow, as shown in Figure 2b. At the reaction time of 20 h, weak peaks were observed at 2θ = 18.58°, 22.56°, 24.41°, 29.81°, 33.76°, and 41.67°, agreeing with spacing of 0.477 nm, 0.393 nm, 0.364 nm, 0.299 nm, 0.265 nm, and 0.216 nm. All these obtained diffraction lines could be identified as cobalt oxalate hydrate crystals through matching and fitting with the standard entire diffraction pattern (JCPDS No. 01-296). The layered structure of V/Co LDH was not clear after the inclusion of oxalate anions among the nanolayers, meaning that the inclusion of oxalate anions caused distortion in the arrangement of the nanolayers. The bulk molecule of oxalate has four oxygen atoms with high electronegativity. Therefore, the strong repulsion forces among the oxalate anions inside the nanolayers pushed the nanolayers, causing them to deviate from their ordered arrangement and leading to an amorphous structure. This means that OXVC-20 consisted of two structures: a disordered structure of V/Co LDH supported with Co-oxalate particles.

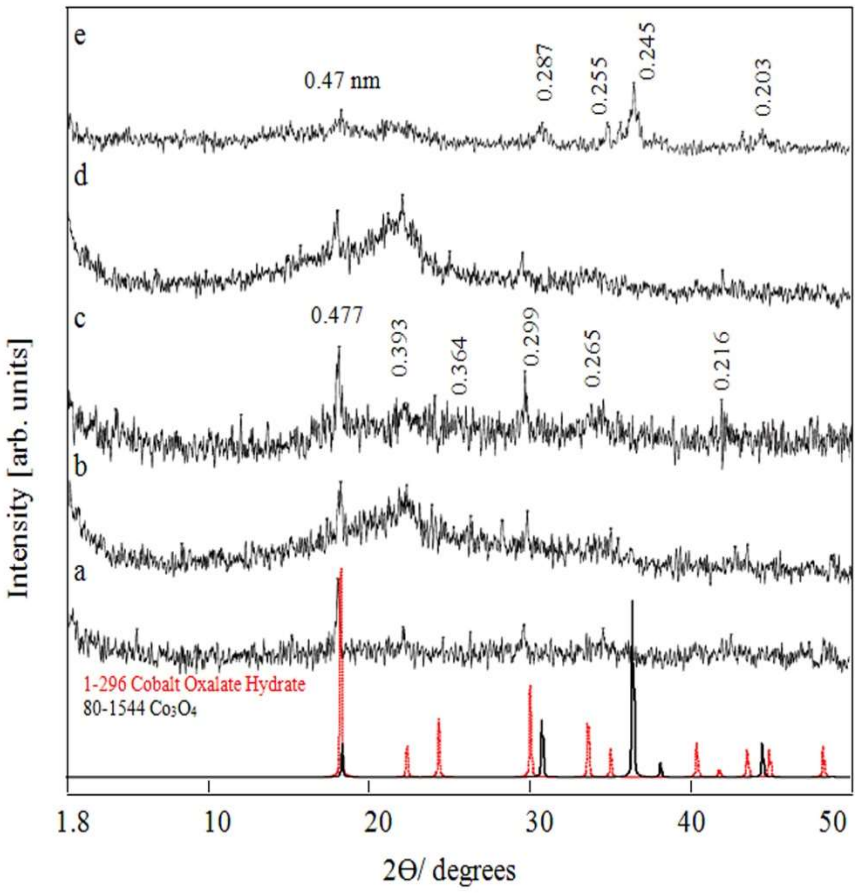

Figure 2. X-ray diffraction of OXVC-20 after various reaction times: (**a**) 6 h, (**b**) 15 h, (**c**) 20 h, (**d**) OXVC-16 after 20 h, and (**e**) OXVC-16 after calcination at 500 °C.

After decreasing the content of oxalate with lower concentrations of vanadium, the XRD pattern of OXVC-16 exhibited lower crystallinity, as shown in Figure 2d. Compared with the layered structure of CNOVC, the layered structure was not clear after the inclusion

of oxalate anions because of the formation of a disordered structure of V/Co LDH. This means that the intercalation of the oxalate molecules inside the nanolayers led to distortion in the layered structure because of the strong repulsion forces among the oxalate anions inside the layered structures.

After calcination of OXVC-16 at 500 °C, new peaks were observed at 2θ = 18.7°, 31.06°, 35.11°, 36.61°, and 44.46°, agreeing with spacing of 0.47 nm, 0.287 nm, 0.255 nm, 0.245 nm, and 0.203 nm, as shown in Figure 2e. All these peaks could be identified as cobalt oxides Co_3O_4 through matching with the standard entire diffraction pattern (JCPDS No. 80-1544) [41]. There was a slight shift from the standard diagram of cobalt oxides because of the inclusion of vanadium inside the crystals of Co_3O_4. No peaks were detected for vanadium, indicating that the vanadium was homogenously dispersed inside the structure of Co_3O_4.

2.3. Fourier Transform Infrared Spectroscopy

The symmetry and nature of the interlayered anions and the functional groups of the prepared materials were recognized by the FT-IR spectra, as seen in Figure 3 and 4. For the CNOVC sample, FT-IR spectra were similar to those generally reported for LDH [42]. Figure 3a shows the spectrum of CNOVC after a reaction time of 6 h. The clear band at 2219 cm^{-1} confirms the presence of cyanate anions through the vibrational mode of CNO. In addition, the band observed at 636 cm^{-1} could be due to the ν_2 form of cyanate anions. The hydroxyl groups were discovered by noticing that the stretching mode of the O–H bonds around 2852 cm^{-1} and 2923 cm^{-1} agreed with the bands of the interlayered water that hydrogen-bonded to the interlayered anions [43]. The presence of water molecules was confirmed through the observation of peaks around 1637 cm^{-1} because of the bending mode of water molecules.

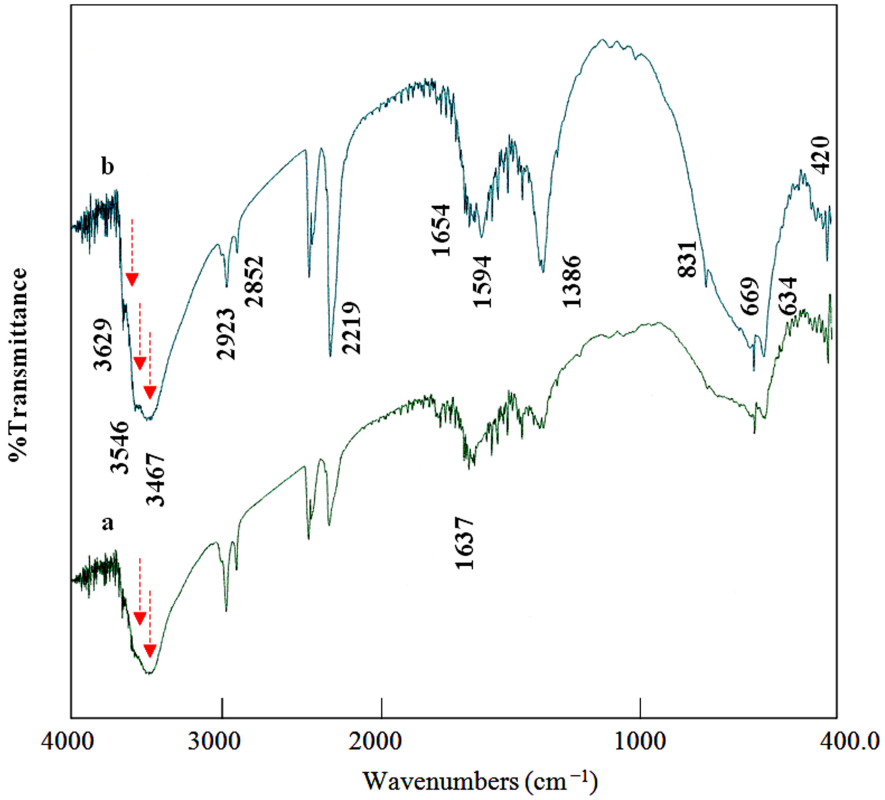

Figure 3. Infrared spectra of CNOVC after different reaction times: (**a**) 6 h and (**b**) 15 h (the red arrows point out different peaks for hydroxyl groups).

The confinement of NCO ions among the nanolayers and beside OH groups showed an important phenomenon agreeing with the results of Xu et al. [44]. The high electron density of NCO causes a strong effect on the vibration of OH groups, and this effect led to the splitting of the hydroxyl bands into two bands around 3500 cm^{-1}, as shown in Figure 3a: one for the OH groups beside the NCO groups at 3451 cm^{-1} and the other for the unaffected OH groups showing an absorption band at 3563 cm^{-1}, as reported for the usual hydroxyl groups. This splitting of the bands of the hydroxyl groups is due to the effect of the cyanide group lowering the electron density of O–H bonds. The results of Xu et al. [44] showed the same phenomenon for the effect of nitrate ions on the bands of LDH. This phenomenon was confirmed and is clearly observed in Figure 3b. When the reaction time was increased to 15 h, the FT-IR spectrum showed that the band of cyanate became sharper and stronger at 2219 cm^{-1}, and carbonate anions appeared as secondary interlayered anions at 1386 cm^{-1}, as shown in Figure 3b. The presence of high cyanate anion content inside the interlayered space showed a strong effect on the vibration of the hydroxyl group, indicating three bands for the hydroxyl groups at 3629 cm^{-1}, 3546 cm^{-1}, and 3467 cm^{-1}.

Figure 4 shows the FT-IR spectrum of the OXVC-20 sample after changing the interlayered anions. The spectrum was very similar to that generally reported for the LDH structure [42]. When compared with CNOVC, both spectra were similar except for the disappearance of the band for cyanate and the appearance of new bands for the oxalate anions. This means that OXVC-20 has an LDH structure. Figure 4 presents a series of bands at 1637 cm^{-1}, 1359 cm^{-1}, 1315 cm^{-1}, 821 cm^{-1}, and 777 cm^{-1}. It can be seen that these bands are due to oxalate anions by comparing them with the standard pattern of oxalate. Also, the presence of oxalate in the interlayered spacing was confirmed by the appearance of hydrogen bond bands at 2925 cm^{-1} and 2854 cm^{-1}, as well as the splitting of the hydroxyl band to one band at 3369 cm^{-1} and a shoulder at 3567 cm^{-1}. This means that the presence of oxalate anions inside the interlayered spacing created hydrogen bonds and caused the lowering of O–H bond electron density.

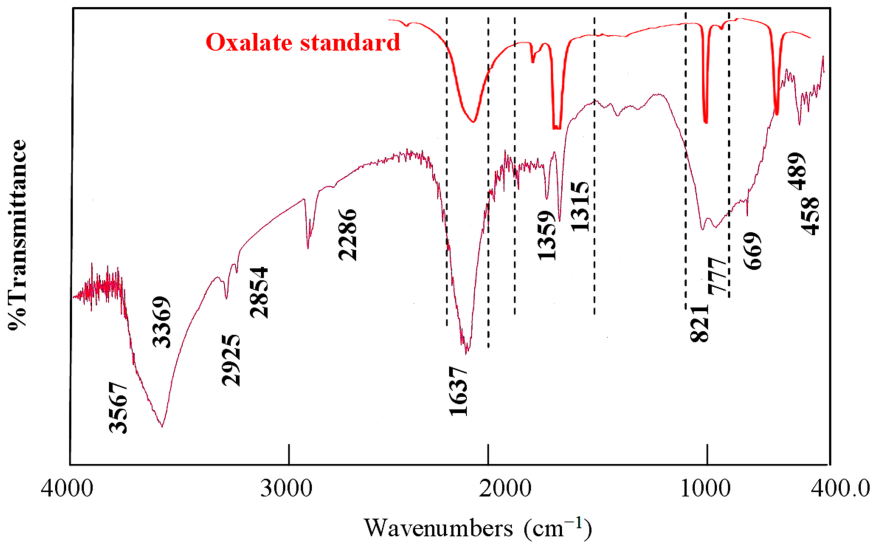

Figure 4. Infrared spectrum of OXVC-20.

2.4. Thermal Analyses

The thermal behavior of the prepared nanolayered materials was studied through measuring thermal gravimetric analysis (TGA), differential thermal analysis (DTA), and differential thermal gravimetric (DTG) analysis. TGA, DTA, and DTG analysis were carried out in the presence of both nitrogen gas and air. For the CNOVC sample, which formed after the reaction time of 6 h and was measured in the presence of nitrogen, curves of TGA, DTG analysis, and DTA are shown in Figure 5a. In the TG curve, two stages of weight loss

can be seen at 209 °C and 343 °C. The first stage represented a 14 wt.% loss of weight and occurred through two steps of the evaporation process of the adsorbed and interlayered water [45]. The removal of the interlayered anions (13 wt.%) happened in the second stage at 343 °C. This stage was confirmed by observing two endothermic peaks in the DTA curve. These peaks occurred at 261 °C and 290 °C, representing the thermal decomposition of the interlayered anions. In addition, these peaks agreed with the two peaks which were observed in the DTG analysis curve at 257 °C and 286 °C. These results suggest that there are two anions in the structure of CNOVC.

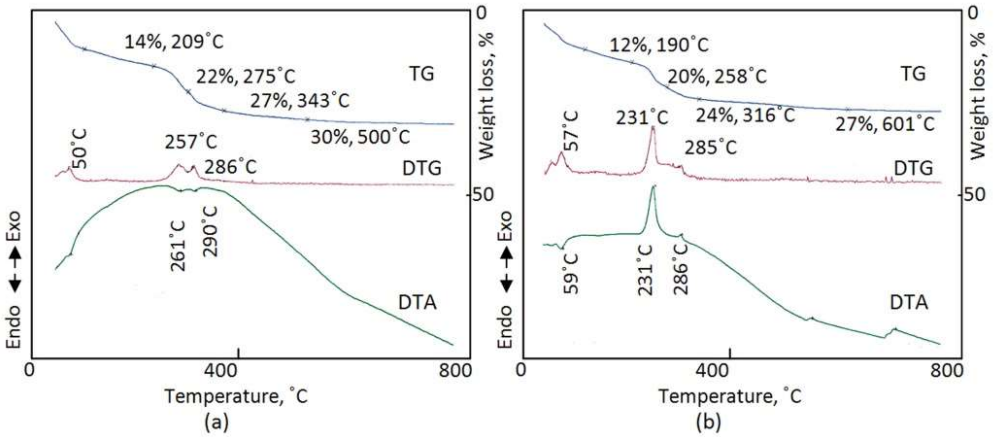

Figure 5. Thermal analyses of CNOVC after a reaction time of 6 h (**a**) in nitrogen gas and (**b**) in air.

Figure 5b presents the TGA, DTG analysis, and DTA curves of CNOVC measured in the presence of laboratory air. The DTA curve revealed exothermic peaks at 231 °C and 286 °C. These peaks confirmed the oxidation reactions of cobalt and vanadium in addition to the reactions of cyanate anions with oxygen in the air. For the DTG analysis and TGA curves, similar results for that of nitrogen gas were observed, as shown in Figure 5b. It can be concluded that the structure of CNOVC consists of two anions and intercalated water.

Figure 6a shows the thermal characteristics of the same CNOVC sample after a reaction time of 15 h in the presence of nitrogen gas. In the TGA curve, the loss of surface and interlayered water, cyanate, and carbonate anions can be seen through four steps [46,47]. The evaporation of 11% water occurred at 184 °C. For the interlayered anions, 8% cyanate was lost at 265 °C and 6% carbonate was lost at 349 °C. The data from the DTG analysis curve confirm the losses of cyanate and carbonate anions because of the two peaks at 248 °C and 288 °C. This agrees with the results of both TGA and DTG analysis. DTA showed two endothermic peaks at 250 °C and 290 °C.

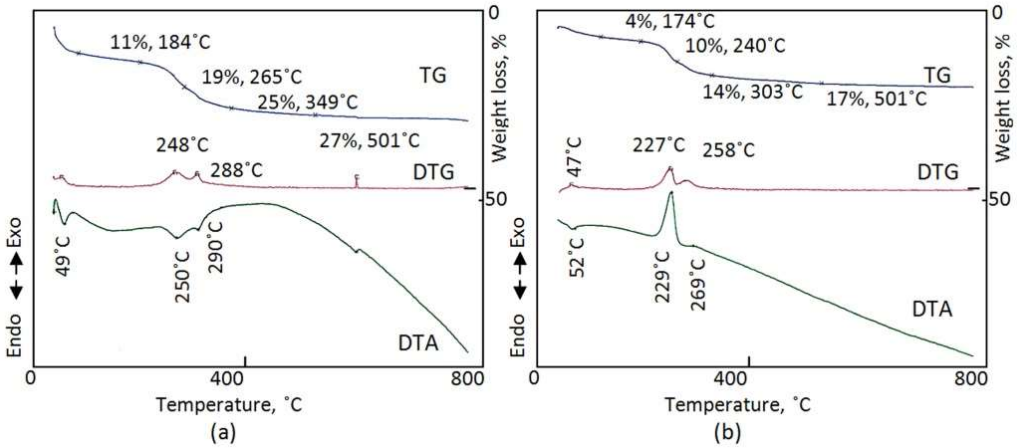

Figure 6. Thermal analyses of CNOVC after a reaction time of 15 h (**a**) in nitrogen and (**b**) in air.

Figure 6b shows the clear effect of oxygen on the different components of the structure of CNOVC in the case of measuring the thermal processes of the CNOVC sample in the presence of air. Five weight losses can be observed with different slopes in the TGA curve. Figure 6b reveals five stages representing five processes: evaporation of both surface and interlayered water, oxidation of cyanate and carbonate anions, and the dehydroxylation process. The oxidation of both cyanate and carbonate anions was confirmed in the DTG analysis curve through the two peaks at 227 °C and 258 °C. In addition, the heat released through the exothermic peaks in the DTA curve at 229 °C and 269 °C confirmed the oxidation reactions.

For OXVC-20, Figure 7 shows the thermal analyses of the sample after reaction times of 6 h and 15 h. The TGA curves indicate that OXVC-20 has two kinds of water and two kinds of oxalate anions, which agrees with the FT-IR data because of the appearance of four weight losses. Surface water comprised 4 wt.% and was lost at 133–141 °C. Subsequently, 11 wt.% of the interlayered water was removed at 190–195 °C. Finally, 18–20 wt.% of the oxalate anions were lost at 439–447 °C through two steps because there are two kinds of oxalate anions, which agrees with the XRD results. DTG analysis and DTA confirmed the TG results through the appearance of two peaks at 167–170 °C and 388–390 °C.

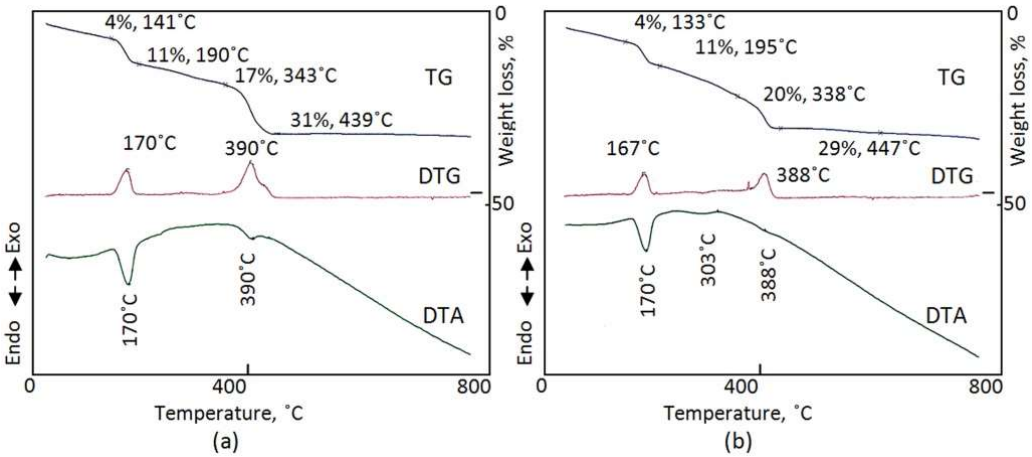

Figure 7. Thermal analyses of OXVC-20 in the presence of nitrogen: (**a**) 6 h and (**b**) 15 h.

2.5. Scanning Electron Microscopy

The imaging technique of scanning electron microscopy (SEM) includes a platinum coating system for the measured samples to increase the resolution of the images. Therefore, thin films of platinum were used to coat the powder samples. Figure 8 shows SEM images of CNOVC. They show that CNOVC has plate-like morphology, agreeing with the literature on LDHs [48–50]. Hexagonal plates were observed for the CNOVC sample, as seen in Figure 8b.

Figure 9 shows SEM images of OXVC-20. They indicate a disordered arrangement for the plates of OXVC-20. The growth of a new phase of cobalt oxalate, in addition to the different orientations of the plates of OXVC-20, created a 3D porous structure, as shown in Figure 9b.

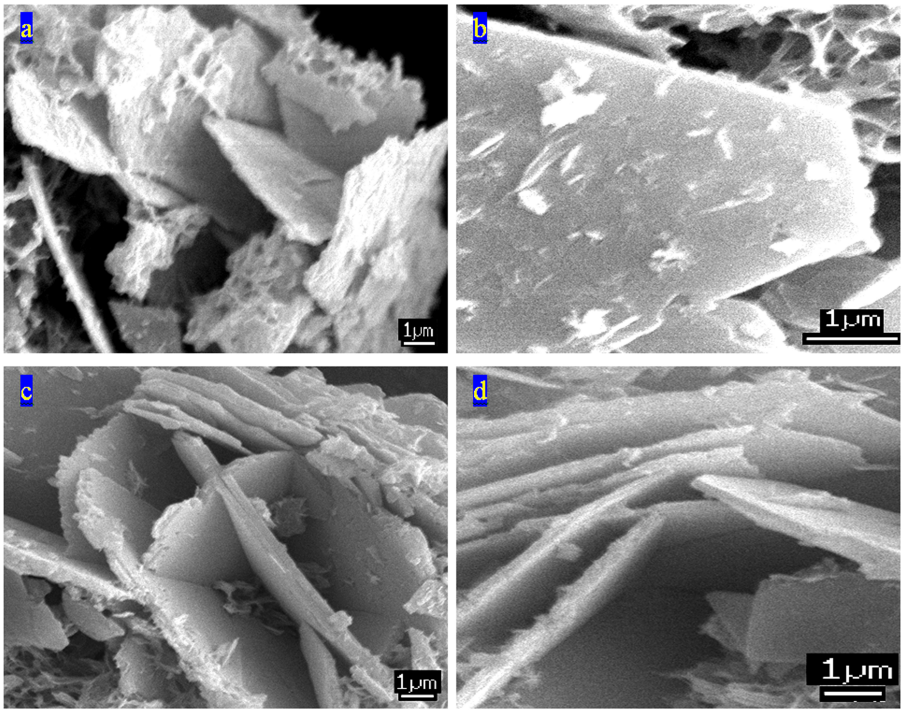

Figure 8. SEM images of CNOVC at different locations: (**a**) the first spot, (**b**) the second spot, (**c**) the third spot, and (**d**) the fourth spot.

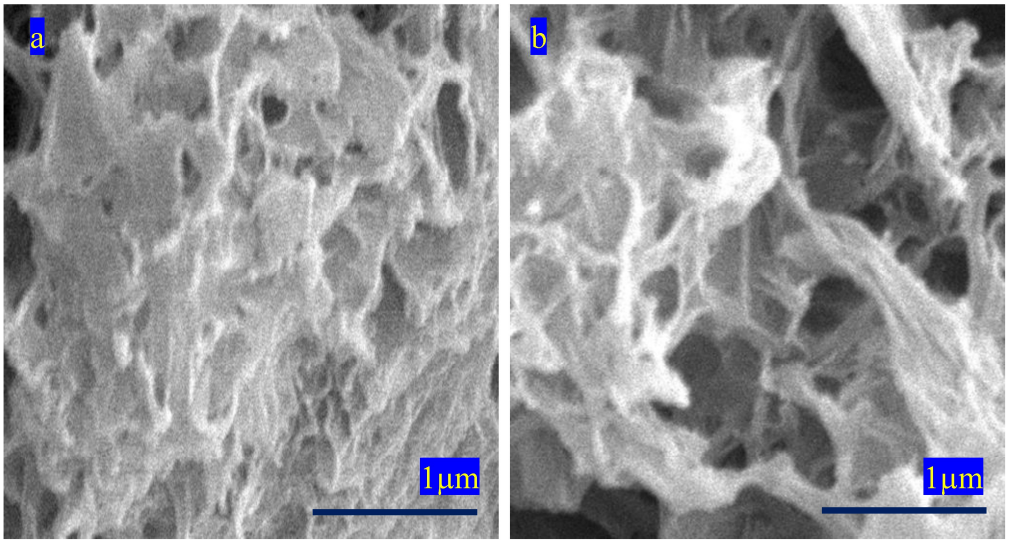

Figure 9. SEM images of OXVC-20 at different locations: (**a**) the first spot and (**b**) the second spot.

2.6. Electrochemical Studies

Three-electrode assembly cells were set up for measurement of the electrochemical performance of the OXVC-20, OXVC-16, OXVC-500, and CNOVC LDH electrodes using cyclic voltammetry and galvanostatic charge–discharge techniques inside the aqueous electrolytes. The initial performance of the electrodes was measured in the potential range of 0.0 V–0.5 V at a scan rate of 5 mV/s, which displayed the redox behavior and further confirmed the Faradic nature of the electrodes. The electrodes were fabricated using experimental conditions such as different ratios of the oxidative and reductive properties. The presence of the cobalt and its oxidative–reductive behavior under the alkaline medium contributed towards the capacitive behavior of the OXVC and CNOVC electrodes. Among

all the electrodes, the OXVC-20 electrode displayed the largest integrated capacitive area inside the CV profile, which contributed to the high electrochemical performance. The enhanced performance of the OXVC-20 electrode could be due to the presence of the synergistic effect contributed by the cobalt and vanadium ions. Another reason could be the different ratios of the dopant, which further modulated the morphology and size of the LDH.

For a better understanding of the electrochemical performance and capacitive nature of the OXVC-20, OXVC-16, OXVC-500, and CNOVC electrodes, the GCD profiles of the electrodes were measured at fixed current and different current loads. The results are presented in Figures 10–12. Figure 10 shows the comparative GCD curves of the OXVC-20, OXVC-16, OXVC-500, and CNOVC electrodes displaying the rapid and fast response, which further confirmed the Faradic behavior of the electrodes. The specific capacitance of each electrode was calculated using the discharge time.

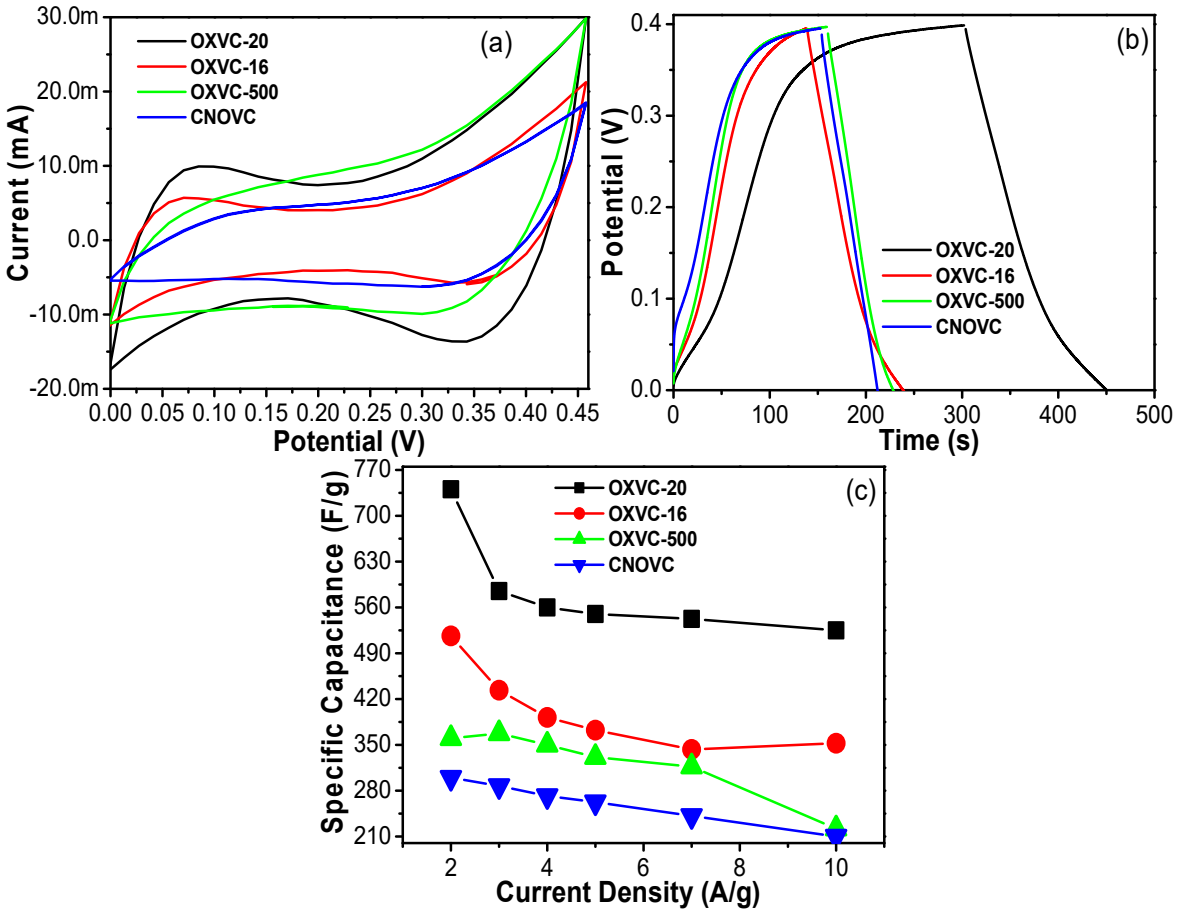

Figure 10. Comparison of (**a**) CV, (**b**) CD, and (**c**) the calculated specific capacitance of all the electrodes (OXVC-20, OXVC-16, OXVC-500, and CNOVC) at different current densities.

The OXVC-20 electrode delivered the highest specific capacitance values of 740.5, 585, 560, 550, 542.5, 525, and 300 F/g at current loads of 2, 3, 4, 5, 7, 10, and 12 A/g, respectively. The OXVC-16 electrode delivered the highest specific capacitance values of 516.5, 433.5, 392, 372.5, 343, 352.5, and 201 F/g at current loads of 2, 3, 4, 5, 7, 10, and 12 A/g, respectively. The OXVC-500 electrode delivered the highest specific capacitance values of 360, 367.5, 350, 331.25, 316.75, 205, and 120 F/g at current loads of 2, 3, 4, 5, 7, 10, and 12 A/g, respectively. The CNOVC electrode delivered the highest specific capacitance values of 300, 287.25, 272, 262.5, 241.5, 210, and 132 F/g at current loads of 2, 3, 4, 5, 7, 10, and 12 A/g, respectively. Based on these results, the OXVC-20 electrode exhibited the highest specific capacitance and longest charge–discharge time owing to its LDH behavior, which provided better active

sites to the electrode and promoted the diffusion of ions inside the structure during the charge –discharge process.

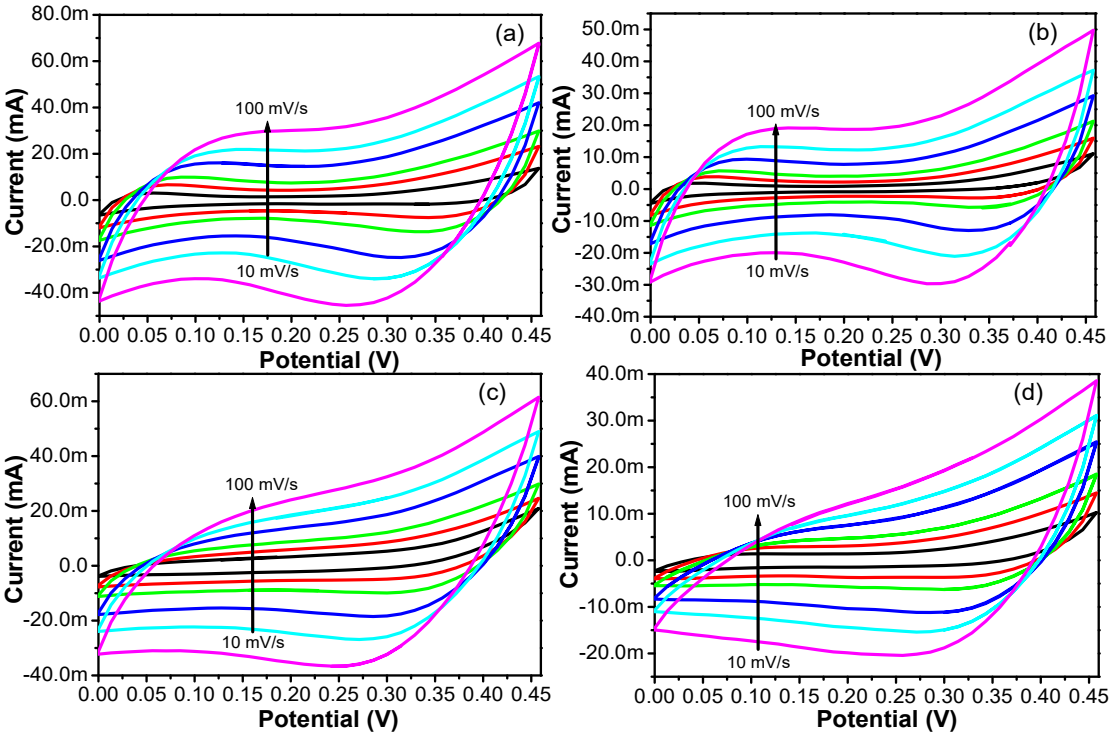

Figure 11. CV of the (**a**) OXVC-20, (**b**) OXVC-16, (**c**) OXVC-500, and (**d**) CNOVC electrodes at different scan rates.

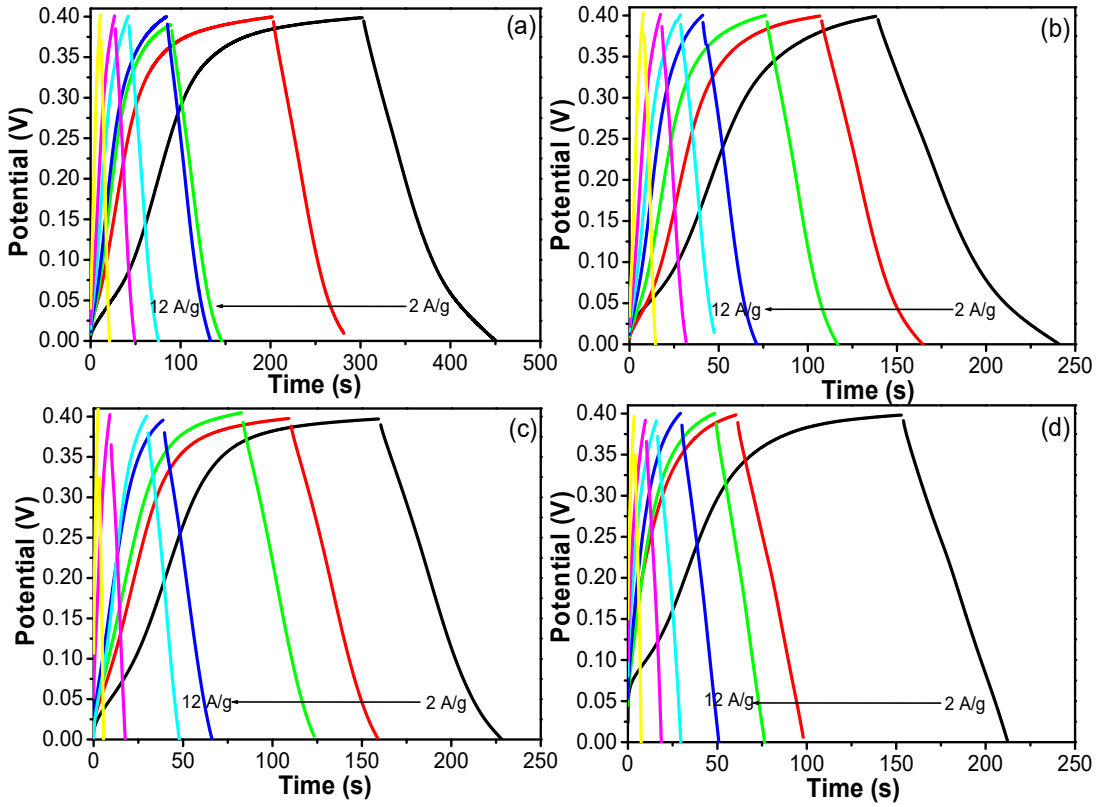

Figure 12. GCD curves of the (**a**) OXVC-20, (**b**) OXVC-16, (**c**) OXVC-500, and (**d**) CNOVC LDH at different current densities (different colors mean different current densities).

The SEM images revealed distinct morphologies for CNOVC and OXVC-20. The plate-like structure of CNOVC and the 3D porous structure of OXVC-20 significantly impact their electrochemical performance. The 3D porous structure of OXVC-20 offers more efficient pathways for ion transport, leading to higher capacitance compared to the more compact, plate-like structure of CNOVC. The chemical composition, specifically the presence of two phases of oxalate in OXVC-20, as shown in the XRD results, plays a crucial role because the oxalate group $(C_2O_4)^{-2}$ creates a framework structure that promotes the diffusion of ions inside the structure during the charge–discharge process. In OXVC-20, the presence of both V/Co-oxalate LDH and Co-oxalate particles enhances its electrochemical properties. In addition, the method of synthesizing these materials, particularly the use of cyanate and oxalate anions as pillars in the nanolayers, also affects their electrochemical characteristics. The anions influence the spacing between layers, the overall stability of the structure, and the ease of ion intercalation, all of which are critical for supercapacitor performance.

Apart from the electrochemical performance measured using CV, GCD, and the corresponding specific capacitance values, the cyclic stability of the electrodes towards various charge–discharge cycles plays an important role in the potential application of the fabricated electrode materials. Figure 13 displays the cyclic stability test graph of the optimized OXVC-20 LDH electrode recorded at a fixed current load of 5 A/g for various charge–discharge cycles. Figure 13 shows that stability initially dropped during the charge–discharge process owing to the saturation of the active site available at the surface of the electrodes. After that, the OXVC-20 electrode displayed 91% capacitance retention after 2300 charge–discharge cycles due to the LDH behavior and size of the electrode materials. The enhanced performance of the prepared materials could be due to the following reasons. The coordination of the metal with the oxygen atoms allowed the metal side to participate in the oxidation and reduction process, whereas the oxygen/oxalate framework provided enough ion diffusion during the charge–discharge process. In addition, the different morphologies played an important role in providing a high surface area and a large number of pores, which provided enough time to complete the redox reaction for ion diffusion during the charge–discharge process. Therefore, we can say that the low-cost, rational framework formed between metal and oxygen and the high surface area of the LDH could be potential contributors to the increased energy storage of the electrode materials.

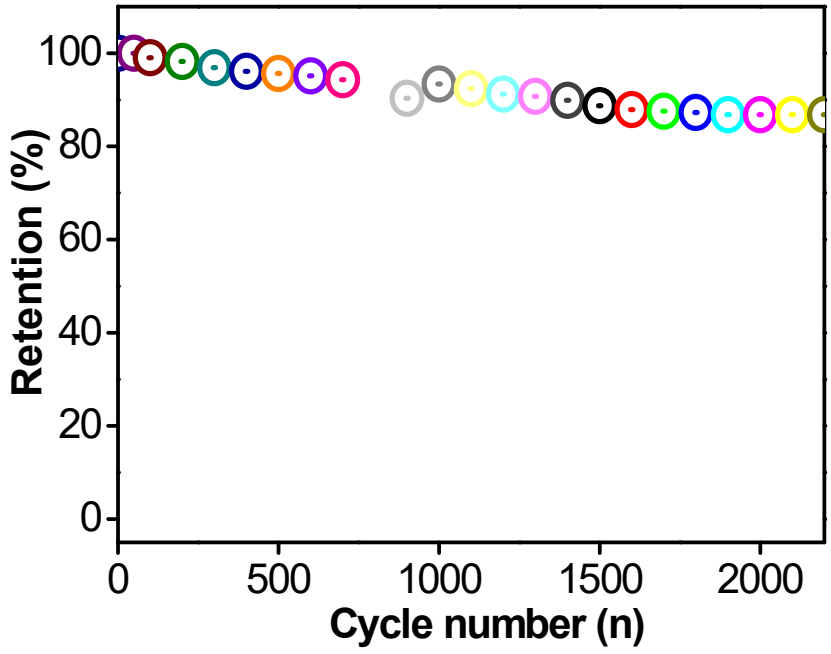

Figure 13. Percent retention performance of the OXVC-20 electrode (different color means new cycle).

3. Materials and Methods

The V/Co LDH was prepared and intercalated by cyanate anions through the slow decomposition of urea. An aqueous and homogeneous solution of both cobalt nitrate and vanadyl dichloride ($VOCl_2$) was mixed with a urea solution under vigorous stirring. Through heating the mixture, the hybrid cyanate/V/Co LDH was precipitated and collected after 6 h and 15 h. The percentage of vanadium was 20 mole%. The product was washed and filtrated several times with distilled water. After drying at room temperature under vacuum, it was labeled as CNOVC.

To build another hybrid structure of oxalate-V/Co, the previous process was repeated using vanadyl oxalate as a precursor for vanadium. Two samples were prepared, with the mole percentages of vanadium being 20% and 16%. The heating of the aqueous solution was continued at 80 °C for 15 h. The samples were coded as OXVC-G, where G is the molar percentage of vanadium.

The elemental analysis was measured using an ICPS-7000 (Shimadzu, Kyoto, Japan). The chemical analysis for carbon, hydrogen, and nitrogen was conducted using the Perkin Elmer CHNS/O 2400II Analyzer. Scanning electron microscopy (SEM) was used for the imaging of products and identification of their morphology through JEOL: JSM-6330F (15 kV/12 mA). X-ray diffraction (XRD) was used for determination of the crystalline structures of the products using a Rigaku RINT 2200 with Cu Kα (filtered) radiation (λ = 0.154 nm) at angles in the range of 1.8° to 50° at 40 kV and 20 mA. Using the KBr disc method, FT-IR spectra were measured using a Horiba FT-720 to determine the functional groups of the products. Thermal behavior was studied through three analyses (TG analysis, DTG analysis, and DTA). The thermal behavior of the powdered samples was measured at up to 800 °C using a Seiko SSC 5200 apparatus under a flow of nitrogen at a heating rate of 10 °C/min.

4. Conclusions

The present study had multiple targets. The first target focused on designing a 2D-nanolayered structure of cyanate-V/Co LDH. In addition, a 2D-nanolayered structure of V/Co was developed by the growth of a new phase of cobalt oxalate to produce a 3D nanostructure using oxalate anions instead of cyanate anions. The main aim concentrated on the behavior of the electrochemical supercapacitance of the different nanostructures of cyanate-V/Co and oxalate-V/Co. The X-ray diffraction, infrared spectra, and thermal analyses confirmed the formation of a 2D-nanolayered structure of cyanate-V/Co. Also, scanning electron microscopy indicated the conversion of 2D nanolayers to a 3D nanostructure. The prepared electrodes delivered excellent capacitance, in which the OXVC-20 electrode delivered a highest specific capacitance of 740.5, the OXVC-16 electrode delivered a highest specific capacitance of 516.5, and the CNOVC electrode delivered a highest specific capacitance of 300 at fixed current load. Based on these results, the OXVC-20 LDH electrode exhibited the highest specific capacitance and longest charge–discharge time owing to its LDH behavior, which provided better active sites to the electrode and promoted the diffusion of ions inside the structure during the charge–discharge process. In addition, the 3D porous structure of OXVC-20 offered more efficient pathways for ion transport leading to higher specific capacitance. Finally, these positive results for the supercapacitance performance of oxalate-V/Co LDH can provide a new additive for the building of active electrodes for high-performance supercapacitor applications.

Author Contributions: Conceptualization, O.S. and S.A.A.; methodology, O.S. and S.A.A.; software, M.O.; validation, N.P., N.M.S. and A.O.; formal analysis, O.S. and S.A.A.; investigation, O.S., N.P. and N.M.S.; resources, M.O.; data curation, A.O.; writing—original draft preparation, O.S. and S.A.A.; writing—review and editing, O.S. and S.A.A.; visualization, M.O.; supervision, O.S. and S.A.A.; project administration, O.S.; funding acquisition, O.S. All authors have read and agreed to the published version of the manuscript.

Funding: This work was supported by the Deanship of Scientific Research, King Faisal University, Saudi Arabia, grant number GRANT4566, and the APC was funded by the same grant number (GRANT4566).

Data Availability Statement: The data presented in this study are available on request from the corresponding author.

Acknowledgments: The authors acknowledge the Deanship of Scientific Research, Vice Presidency for Graduate Studies and Scientific Research, King Faisal University, for financial support through Grant No. GRANT4566.

Conflicts of Interest: The authors declare no conflict of interest.

References

1. Li, M.M.-J.; Chen, C.; Ayvalı, T.; Suo, H.; Zheng, J.; Teixeira, I.F.; Ye, L.; Zou, H.; O'Hare, D.; Tsang, S.C.E. CO_2 hydrogenation to methanol over catalysts derived from single cationic layer CuZnGa LDH precursors. *ACS Catal.* **2018**, *8*, 4390–4401. [CrossRef]
2. Iftekhar, S.; Srivastava, V.; Sillanpaa, M. Synthesis and application of LDH intercalated cellulose nanocomposite for separation of rare earth elements (REEs). *Chem. Eng. J.* **2017**, *309*, 130–139. [CrossRef]
3. Cao, Z.; Adnan, N.N.M.; Wang, G.; Rawal, A.; Shi, B.; Liu, R.; Liang, K.; Zhao, L.; Gooding, J.J.; Boyer, C. Enhanced colloidal stability and protein resistance of layered double hydroxide nanoparticles with phosphonic acid-terminated PEG coating for drug delivery. *J. Colloid Interface Sci.* **2018**, *521*, 242–251. [CrossRef] [PubMed]
4. Sanati, S.; Rezvani, Z. g-C3N4 nanosheet @ CoAl-layered double hydroxide composites for electrochemical energy storage in supercapacitors. *Chem. Eng. J.* **2019**, *362*, 743–757. [CrossRef]
5. Liu, N.; Lin, J.; Wu, J.; Huang, M.; Fan, L.; Song, Z.; Geng, C.; Zhu, T.; Pan, W. Application of CoV-LDH nano-flower in asymmetric supercapacitors with high electrochemical properties. *Electrochim. Acta* **2020**, *336*, 135550. [CrossRef]
6. Long, X.; Wang, Z.; Xiao, S.; An, Y.; Yang, S. Transition metal based layered double hydroxides tailored for energy conversion and storage. *Mater. Today* **2016**, *19*, 213–226. [CrossRef]
7. Hou, Y.; Lohe, M.R.; Zhang, J.; Liu, S.; Zhuang, X.; Feng, X. Vertically oriented cobalt selenide/NiFe layered-double-hydroxide nanosheets supported on exfoliated graphene foil: An efficient 3D electrode for overall water splitting. *Energy Environ. Sci.* **2016**, *9*, 478–483. [CrossRef]
8. Lu, Y.; Jiang, B.; Fang, L.; Ling, F.; Wu, F.; Hu, B.; Meng, F.; Niu, K.; Lin, F.; Zheng, H. An investigation of ultrathin nickel-iron layered double hydroxide nanosheets grown on nickel foam for high-performance supercapacitor electrodes. *J. Alloys Compd.* **2017**, *714*, 63–70. [CrossRef]
9. Zai, J.; Liu, Y.; Li, X.; Ma, Z.-F.; Qi, R.; Qian, X. 3D hierarchical Co–Al layered double hydroxides with long-term stabilities and high rate performances in supercapacitors. *Nano-Micro Lett.* **2017**, *9*, 21. [CrossRef]
10. Li, M.; Cheng, J.; Wang, J.; Liu, F.; Zhang, X. The growth of nickel-manganese and cobalt-manganese layered double hydroxides on reduced graphene oxide for supercapacitor. *Electrochim. Acta* **2016**, *206*, 108–115. [CrossRef]
11. Tang, J.; Shen, Y.; Miao, X.; Qin, H.; Song, D.; Li, Y.; Qu, Y.; Yin, Z.; Ren, J.; Wang, L. Template-directed growth of hierarchically structured MOF-derived LDH cage hybrid arrays for supercapacitor electrode. *J. Electroanal. Chem.* **2019**, *840*, 174–181. [CrossRef]
12. Li, J.; Wei, M.; Chu, W.; Wang, N. High-stable α-phase NiCo double hydroxide microspheres via microwave synthesis for supercapacitor electrode materials. *Chem. Eng. J.* **2017**, *316*, 277–287. [CrossRef]
13. Zhou, Y.; Li, J.; Yang, Y.; Luo, B.; Zhang, X.; Fong, E.; Chu, W.; Huang, K. Unique 3D flower-on-sheet nanostructure of NiCo LDHs: Controllable microwave-assisted synthesis and its application for advanced supercapacitors. *J. Alloys Compd.* **2019**, *788*, 1029–1036. [CrossRef]
14. Jing, M.; Hou, H.; Banks, C.E.; Yang, Y.; Zhang, Y.; Ji, X. Alternating voltage introduced NiCo double hydroxide layered nanoflakes for an asymmetric supercapacitor. *ACS Appl. Mater. Interfaces* **2015**, *7*, 22741–22744. [CrossRef]
15. Hou, L.; Du, Q.; Su, L.; Di, S.; Ma, Z.; Chen, L.; Shao, G. Ni-Co layered double hydroxide with self-assembled urchin like morphology for asymmetric supercapacitors. *Mater. Lett.* **2019**, *237*, 262–265. [CrossRef]
16. Jiang, Z.; Li, Z.; Qin, Z.; Sun, H.; Jiao, X.; Chen, D. LDH nanocages synthesized with MOF templates and their high performance as supercapacitors. *Nanoscale* **2013**, *5*, 11770–11775. [CrossRef] [PubMed]
17. Tyagi, A.; Joshi, M.C.; Agarwal, K.; Balasubramaniam, B.; Gupta, R.K. Three-dimensional nickel vanadium layered double hydroxide nanostructures grown on carbon cloth for high-performance flexible supercapacitor applications. *Nanoscale Adv.* **2019**, *1*, 2400–2407. [CrossRef]
18. Sahoo, R.; Lee, T.H.; Pham, D.T.; Luu, T.H.T.; Lee, Y.H. Fast-Charging High-Energy Battery–Supercapacitor Hybrid: Anodic Reduced Graphene Oxide–Vanadium(IV) Oxide Sheet-on-Sheet Heterostructure. *ACS Nano* **2019**, *13*, 10776–10786. [CrossRef]
19. Wan, F.; Niu, Z. Design Strategies for Vanadium-based Aqueous Zinc-Ion Batteries. *Angew. Chem. Int. Ed.* **2019**, *58*, 16358–16367. [CrossRef]
20. Cheng, Y.; Xia, Y.; Chen, Y.; Liu, Q.; Ge, T.; Xu, L.; Mai, L. Vanadium-based nanowires for sodium-ion batteries. *Nanotechnology* **2019**, *30*, 192001. [CrossRef]

21. Xu, X.; Xiong, F.; Meng, J.; Wang, X.; Niu, C.; An, Q.; Mai, L. Vanadium-Based Nanomaterials: A Promising Family for Emerging Metal-Ion Batteries. *Adv. Funct. Mater.* **2020**, *30*, 1904398. [CrossRef]
22. Shao, M.; Deng, J.; Zhong, F.; Cao, Y.; Ai, X.; Qian, J.; Yang, H. An all-vanadium aqueous lithium ion battery with high energy density and long lifespan. *Energy Storage Mater.* **2019**, *18*, 92–99. [CrossRef]
23. Zand, Z.; Salimi, P.; Mohammadi, M.R.; Bagheri, R.; Chernev, P.; Song, Z.; Dau, H.; Gorlin, M.; Najafpour, M.M. Nickel-Vanadium Layered Double Hydroxide under Water-Oxidation Reaction: New Findings and Challenges. ACS Sustain. *Chem. Eng.* **2019**, *7*, 17252–17262. [CrossRef]
24. Zhou, P.; Wang, C.; Liu, Y.; Wang, Z.; Wang, P.; Qin, X.; Zhang, X.; Dai, Y.; Whangbo, M.-H.; Huang, B. Sulfuration of NiV-layered double hydroxide towards novel supercapacitor electrode with enhanced performance. *Chem. Eng. J.* **2018**, *351*, 119–126. [CrossRef]
25. Gonçalves, J.M.; Martins, P.R.; Araki, K.; Angnes, L. Recent progress in water splitting and hybrid supercapacitors based on nickel-vanadium layered double hydroxides. *J. Energy Chem.* **2021**, *57*, 496–515. [CrossRef]
26. Gonçalves, J.M.; da Silva, M.I.; Toma, H.E.; Angnes, L.; Martins, P.R.; Araki, K. Trimetallic oxides/hydroxides as hybrid supercapacitor electrode materials: A review. *J. Mater. Chem.* **2020**, *8*, 10534–10570. [CrossRef]
27. Wu, Z.; Khalafallah, D.; Teng, C.; Wang, X.; Zou, Q.; Chen, J.; Zhi, M.; Hong, Z. Vanadium doped hierarchical porous nickel-cobalt layered double hydroxides nanosheet arrays for high-performance supercapacitor. *J. Alloys Compd.* **2020**, *838*, 155604. [CrossRef]
28. Lee, S.C.; Kim, M.; Park, J.H.; Kim, E.S.; Liu, S.; Chung, K.Y.; Jun, S.C. An unexpected phase-transformation of cobalt–vanadium layered double hydroxides toward high energy density hybrid supercapacitor. *J. Power Source* **2021**, *486*, 229341. [CrossRef]
29. Qu, C.; Jiao, Y.; Zhao, B.; Chen, D.; Zou, R.; Walton, K.S.; Liu, M. Nickel-based pillared MOFs for high-performance supercapacitors: Design, synthesis and stability study. *Nano Energy* **2016**, *26*, 66–73. [CrossRef]
30. Liu, X.; Shi, C.; Zhai, C.; Cheng, M.; Liu, Q.; Wang, G. Cobalt-based layered metal–organic framework as an ultrahigh capacity supercapacitor electrode material. *ACS Appl. Mater. Interfaces* **2016**, *8*, 4585–4591. [CrossRef] [PubMed]
31. Du, P.; Dong, Y.; Liu, C.; Wei, W.; Liu, D.; Liu, P. Fabrication of hierarchical porous nickel based metal-organic framework (Ni-MOF) constructed with nanosheets as novel pseudo-capacitive material for asymmetric supercapacitor. *J. Colloid Interface Sci.* **2018**, *518*, 57–68. [CrossRef]
32. Fu, H.-R.; Xu, Z.-X.; Zhang, J. Water-stable metal–organic frameworks for fast and high dichromate trapping via single-crystal-to-single-crystal ion exchange. *Chem. Mater.* **2015**, *27*, 205–210. [CrossRef]
33. Liu, K.; Sun, Y.; Deng, L.; Cao, F.; Han, J.; Wang, L. Cu (II) coordination polymers constructed by tetrafluoro terephthalic acid and varied imidazole-containing ligands: Syntheses, structures and properties. *J. Solid State Chem.* **2018**, *258*, 24–31. [CrossRef]
34. Du, M.; Li, C.-P.; Liu, C.-S.; Fang, S.-M. Design and construction of coordination polymers with mixed-ligand synthetic strategy, Coord. *Chem. Rev.* **2013**, *257*, 1282–1305.
35. D'Amato, R.; Donnadio, A.; Carta, M.; Sangregorio, C.; Tiana, D.; Vivani, R.; Taddei, M.; Costantino, F. Water-based synthesis and enhanced CO_2 capture performance of perfluorinated cerium-based metal-organic frameworks with UiO-66 and MIL-140 topology. *ACS Sustain. Chem. Eng.* **2018**, *7*, 394–402. [CrossRef]
36. Yadav, B.; Trivedi, M.; Yadav, A.K.; Singh, G.; Kumar, A.; Kumar, G.; Husain, A.; Rath, N. Synthetic, spectral, structural and catalytic activity of infinite 3-D and 2-D copper (ii) coordination polymers for substrate size-dependent catalysis for CO_2 conversion. *Dalton Trans.* **2019**, *48*, 10078–10088.
37. Lou, X.; Hu, X.; Li, C.; Ning, Y.; Chen, Q.; Shen, M.; Hu, B. Room-temperature synthesis of a cobalt 2,3,5,6-tetra fluoroterephthalic coordination polymer with enhanced capacity and cycling stability for lithium batteries. *New J. Chem.* **2017**, *41*, 1813–1819. [CrossRef]
38. Saber, O.; Aljaafari, A.; Asiri, S.; Batoo, K.M. Designing Magnetic Layered Double Hydroxides and Two-Dimensional Magnetic Nano-Nets of Cobalt Ferrite through a Novel Approach. *Appl. Sci.* **2018**, *8*, 2099. [CrossRef]
39. Saber, O.; Aljaafari, A.; Osama, A.; Alshoaibi, A. Optimization Conditions for Crystal Growth of Novel Nanolayers, Nanohybrids and Nanocomposites Based on Cobalt, Zirconium, Titanium and Silicon. *ChemistrySelect* **2019**, *4*, 580–588. [CrossRef]
40. Zhang, Q.; Xu, Y.; Li, C.; Chen, W.; Zhu, W.; Wang, L. Staggered nickel–vanadium layered double hydroxide nanosheets on reduced graphene oxide via in-situ growth for enhanced supercapacitor performance. *J. Alloys Compd.* **2023**, *935*, 168048. [CrossRef]
41. Amutha, R.; Akilandeswari, S.; Muruganandham, M.; Sillanpää, M.; Ahmmad, B.; Ohkubo, T. Template-free synthesis of self-assembly Co_3O_4 micro/nanocrystals. *J. Nanosci. Nanotechnol.* **2011**, *11*, 3171–3179. [CrossRef] [PubMed]
42. Saber, O.; Osama, M.; Alshoaibi, A.; Shaalan, N.M.; Osama, D. Designing inorganic–magnetic–organic nanohybrids for producing effective photocatalysts for the purification of water. *RSC Adv.* **2022**, *12*, 18282–18295. [CrossRef]
43. Miyata, S. The syntheses of hydrotalcitelike compounds and their structures and physicochemical properties. *Clays Clay Miner.* **1995**, *23*, 369–375. [CrossRef]
44. Xu, Z.P.; Zeng, H.C. Decomposition Pathways of Hydrotalcite-like Compounds $Mg_{1-x}Al_x(OH)_2(NO_3)_X{\cdot}nH_2O$ as a Continuous Function of Nitrate Anions. *Chem. Mater.* **2001**, *13*, 4564–4572. [CrossRef]
45. Constantino, V.R.L.; Pinnavaia, T.J. Basic Properties of Mg2+ 1−xAl3+ x Layered Double Hydroxides Intercalated by Carbonate, Hydroxide, Chloride, and Sulfate Anions. *Inorg. Chem.* **1995**, *34*, 883–892. [CrossRef]
46. Saber, O.; Ansari, S.A.; Alshoaibi, A. Development of Ti/Ni Nanolayered Structures to Be a New Candidate for Energy Storage Applications. *Appl. Sci.* **2020**, *10*, 6935. [CrossRef]

47. Saber, O.; Aljaafari, A.; Alomair, H.A.; Alshoaibi, A. Novel Strategy for Producing Nanoplatelets to be Used as Building Blocks for Shaping Nanofibers through Layered Double Hydroxides and Poly Vinyl Alcohol. *ChemistrySelect* **2019**, *4*, 4293–4300. [CrossRef]
48. Benito, P.; Guinea, I.; Labajos, F.M.; Rives, V. Microwave-hydrothermally aged Zn, Al hydrotalcite-like compounds: Influence of the composition and the irradiation conditions. *Microporous Mesoporous Mater.* **2008**, *110*, 292–302. [CrossRef]
49. Benito, P.; Herrero, M.; Barriga, C.; Labajos, F.M.; Rives, V. Microwave-assisted homogeneous precipitation of hydrotalcites by urea hydrolysis. *Inorg. Chem.* **2008**, *47*, 5453–5463. [CrossRef]
50. Chang, P.-H.; Chang, Y.-P.; Chen, S.-Y.; Yu, C.-T.; Chyou, Y.-P. Ca-rich Ca-Al-oxide, high-temperature-stable sorbents prepared from hydrotalcite precursors: Synthesis, characterization, and CO_2 capture capacity. *Chem. Sus. Chem.* **2011**, *4*, 1844–1851. [CrossRef]